Balance of Solvent and Chain Interactions Determines the Local Stress State of Simulated Membranes

Conner M. Winkeljohn,[†] Benjamin Himberg,[‡] and Juan M. Vanegas[*,†,‡]

†*Department of Physics, University of Vermont, Burlington, Vermont 05405, USA*

‡*Materials Science Graduate Program, University of Vermont, Burlington, Vermont 05405, USA*

E-mail: jvanegas@uvm.edu

Phone: +1 802 6560049

Abstract

Characterization of the internal mechanical state of model lipid membranes is essential to understand the microscopic underpinnings of biological functions such as membrane fission and organelle shaping within the context of elastic theories such as the Helfrich framework. Here, we compute lateral stress or pressure profiles from molecular dynamics simulations of lipid bilayers and water-vacuum interfaces to understand the role that solvent treatment and force-field parametrization plays on the local mechanical features of membranes. We focus on two atomistic models, GROMOS 43A1-S3 and CHARMM36, and several variants of the MARTINI coarse-grained force-field, including the single-bead non-polar water, three-point polarizable water, big multipole water, and solvent-free. Our results show that the various atomistic and coarse-grained force-fields produce contrasting lateral stress profiles as a result of the balance of solvent-solvent and solvent-solute forces at the hydrocarbon-water interface and fundamentally different treatment of pairwise (e.g., van der Waals, Coulomb, etc.) and multi-body interactions (angles and torsions). Numerical integration of the second moment of the bilayer stress profiles indicates that different local distributions of repulsive and attractive stresses across the membrane, due to distinct force-field parametrizations, may result in substantial variations in macroscopic elastic properties.

Introduction

The physical properties of aqueous interfaces determine the behavior of many essential biological components such as lipid membranes, where a delicate balance of solvent and solute interactions drive spontaneous self-assembly of individual molecules in arrangements with particular geometries. Beyond their role in compartmentalization and segregation of biological processes, lipid membranes are also essential players in numerous mechanically-coupled biological functions including membrane fission and fusion,[1,2] organelle and cellular shaping,[1–3] osmotic regulation,[4,5] and mechanical signal transduction[4,6–11] among others. Under-

standing its role in each of these processes requires careful characterization of the internal mechanical state of the membrane, which is typically described by the lateral stress, $\sigma_{\mathrm{L}}(z)$, or pressure, $\pi(z) = -\sigma_L(z)$, profile. Stress profiles provide an average description of the local balance of forces along the direction normal to the membrane plane $(x - y)$ and can be directly obtained from molecular dynamics (MD) simulations through calculation of the microscopic or local stress tensor, $\boldsymbol{\sigma}$, by taking the difference between lateral and normal components, $\sigma_{\mathrm{L}}(z) = \sigma_{xx}(z) - \sigma_{zz}(z)$, where $\sigma_{xx} = \sigma_{yy}$. Within the general Helfrich framework of membrane mechanics,[12–19] the local stress and elasticity tensors provide microscopic underpinnings to elastic constants such as the bending and Gaussian curvature moduli. In addition to elastic properties, it has been proposed by Cantor and others[12,20,21] that membrane protein function is modulated by the repulsive and attractive tensions described by the stress profile, which has been suggested to depend on membrane composition[22] due to differences in lipid chemical structure and affected by partitioning of other molecules such as anesthetics.[20]

The stress tensor from MD simulations is spatially defined from the particle interaction forces and velocities within the Irving-Kirkwood-Noll (IKN) statistical mechanics theory.[23–29] A key step in the IKN procedure is the decomposition of forces from multi-body potentials, such as those that constrain angles and torsions, into pairwise forces to obtain the stress tensor. In previous studies,[30–32] we and others have shown that the central force decomposition (CFD) method[29,31] produces physically sound stress tensors from MD simulations that are always symmetric by construction and in good agreement with general theoretical expectations.[12,33] Furthermore, local stress analysis with the CFD method has shown that internal molecular features such as rigid double bonds in unsaturated lipids such as POPC (1-palmitoyl-2-oleoyl-glycero-3-phosphocholine) can result in large repulsive stress peaks in the bilayer core in contrast to that observed in saturated lipids such as DPPC (1,2-dipalmitoyl-glycero-3-phosphocholine). While obtaining experimental measurements of lateral stress within a membrane is very challenging, fluorescence studies using di-pyrene

labeled lipids in DOPC (1,2-dioleoyl-glycero-3-phosphocholine) membranes have shown that the ratio of excimer to monomer intensity, a proxy for the lateral stress, varies drastically according to the position of the fluorescent label along the lipid chain relative to the double bond.[34]

Here, we explore the role that force-field (FF) parametrization plays on the observed internal mechanical state of lipid membranes, through local stress calculations, by comparing systems with varying solvent descriptions and molecular features. In the first section, we focus on two atomistic lipid models, GROMOS 43A1-S3[35] and CHARMM36,[36,37] that have been shown to reproduce many important bilayer properties such as area per molecule, deuterium order parameters, and scattering data.[35–38] We selected these two from the numerous atomistic FFs available in the literature, such as Slipids,[39] Berger,[40] and AMBER[41] among others, as they were developed with different water models (SPCE[42] vs. TIP3P[43]) and parametrized completely independent of each other. As stress profiles are frequently used to assess whether coarse-grained models reproduce the mechanical properties of atomistic systems,[21,44–46] the second section focuses on local stress analysis of coarse-grained (CG) models including a variety of explicit and implicit solvents based on the popular MARTINI FF.[44,47] The original and most common flavor of MARTINI uses a single non-polar bead to represent water, which although very computationally efficient fails to capture many important electrostatic effects due to the lack of charged interactions. A three-point polarizable water model (Pol-MARTINI[48]) was later introduced to address some short-comings of the more basic parametrization, and other CG solvents such as the big multipole water (BMW) model[49] have been combined with MARTINI to improve membrane-protein interactions.[50] More recently, a solvent-free variant, Dry-MARTINI,[51] was developed to dramatically increase computationally efficiency and achieve simulations that span much larger length and time scales. We show that the various atomistic and CG force-fields produce contrasting lateral stress profiles as a result of the balance of forces at the hydrocarbon-water interface and fundamentally different treatment of pairwise (van der Waals, Coulomb, etc.) and multi-

body interactions (angles and torsions). We also show by numerical integration of the second moment of the stress profiles that these different FFs may present substantial variations in macroscopic elastic properties.

Methods

Lipid Bilayer Simulations

Simulations of lipid bilayers composed of 200 DPPC (1,2-dipalmitoyl-sn-glycero-3-phosphocholine) or POPC (1-palmitoyl-2-oleoyl-sn-glycero-3-phosphocholine) molecules were conducted with the GROMACS simulation package[52–54] versions 4.5.7 and 2016.3. The number of water molecules in the atomistic systems were 12,000 to provide a ratio of 60 waters/lipid. Atomistic simulations with the GROMOS 43A1-S3[35] force-field (FF) and SPCE[42] water model were taken from Vanegas et al.[30] Briefly, for G43A1-S3/SPCE simulations, Lennard-Jones (LJ) forces where calculated using a twin-range cut-off scheme with interactions within 1.0 nm calculated at every time step and interactions between 1.0 and 1.6 nm only updated every 5 time steps. Long-range electrostatic interactions were computed using the particle-mesh Ewald (PME) method with a real-space cut-off of 1.0 nm and a Fourier grid spacing of 0.15 nm. For atomistic simulations with the CHARMM36[36,37] lipid FF, LJ forces where calculated using a force-switching function from 1.0 to 1.2 nm. Long-range electrostatic interactions were computed using the PME method with a real-space cut-off of 1.2 nm and a Fourier grid spacing of 0.12 nm. Three different sets of simulations were completed for the C36 FF: i) using the CHARMM modified TIP3P water model that includes additional LJ interactions for hydrogen atoms (labeled mTIP3P) under constant pressure (NPT), ii) using the standard TIP3P water model (labeled sTIP3P) under constant pressure (NPT), and iii) using the standard TIP3P water model under constant area (NP_zAT). Atomistic systems under constant pressure were semi-isotropically coupled to a Parrinello-Rahman barostat at 1 atm, temperature was held constant at 50 °C with a Nosé-Hoover thermostat, and the

integration time step was 2 fs. Systems were run for a 400 ns equilibration period followed by 200 ns of data collection (saving the trajectory every 5 ps).

Similarly to the atomistic membranes, lipid bilayers composed of 200 DPPC and 200 POPC lipids were simulated with four different flavors of the popular MARTINI CG FF[44,47] each with different solvent treatments. The three explicit-solvent variants include the conventional MARTINI model with 1 bead non-polar solvent, Pol-MARTINI with the 3-bead polarizable water model,[48] and BMW-MARTINI,[50] a re-parametrization of the MARTINI FF based on the big multipole water (BMW) model.[49] The remaining CG model is the newly developed implicit-solvent Dry-MARTINI.[51] For the explicit-solvent CG membranes, the chosen number of water molecules was 3,000 to have the same effective ratio of 60 'real' waters per lipid given the 1 to 4 mapping between atomistic and CG waters. For MARTINI, Pol-MARTINI, and Dry-MARTINI, LJ forces where calculated using a shifted potential with a cut-off of 1.1 nm and electrostatic interactions were computed using a shifted Coulombic potential with cut-off radius of 1.1 nm. For MARTINI and Dry-MARTINI the relative permitivity constant was set to $\epsilon_r = 15$ and for Pol-MARTINI it was set to $\epsilon_r = 2.5$. For BMW-MARTINI, LJ forces where calculated using a shifted potential with a cut-off of 1.4 nm and long-range electrostatic interactions were computed using the PME method with a cutoff of 1.4 nm and a Fourier grid spacing of 0.2 nm. All CG systems were simulated under constant pressure with semi-isotropic coupling to a Parrinello-Rahman barostat at 1 atm. Compressibility of the Dry-MARTINI membranes in the z-direction was set to 0 in order to keep the z dimension from changing. Temperature was held constant at 50 °C with a velocity-rescaling thermostat[55] for MARTINI, Pol-MARTINI, and BMW-MARTINI, while Dry-MARTINI was simulated with a stochastic dynamics integrator with a friction time constant of 4.0 ps. The integration time step for all CG systems was 20 fs except for Dry-MARTINI were a 40 fs step was used. CG systems were run for a 200 ns equilibration period followed by 200 ns of data collection (saving positions and velocities the trajectory every 5 ps).

Water-Vacuum Simulations

Simulations of liquid water-vacuum interfaces for all atomistic and CG models were conducted with the same simulation parameters as the corresponding lipid bilayers with the exception of pressure coupling were the box size was kept constant. For atomistic systems, the simulation box had a z dimension of 16 nm and contained 12,000 water molecules resulting in a liquid layer ~ 8 nm and vacuum separation of ~ 8 nm. Similarly for CG systems, the box z dimension was fixed at 13 nm and the system contained enough waters to have a liquid layer of ~ 8 nm with a ~ 5 nm vacuum gap. Water-vacuum simulations were run for a total of 300 ns each, with analysis conducted over the last 200 ns (positions and velocities saved every 5 ps). Surface tension for these constant volume simulations was calculated from the total pressure tensor ($\boldsymbol{P}$, obtained from the total kinetic energy and the virial tensors of the system) and the box length along the interface (L_{zz})

$$\gamma = \frac{L_{zz}}{2}\left[P_{zz} - \frac{(P_{xx}+P_{yy})}{2}\right]. \tag{1}$$

Local Stress Analysis

The local stress tensor ($\boldsymbol{\sigma}$) was calculated using the Irving-Kirkwood-Noll procedure[23,24,27,56,57] with forces from multibody potentials decomposed into pairwise terms using the central force decomposition (CFD) methodology.[30–32,58] Briefly, the simulation volume is divided into uniform blocks and the local stress tensor is calculated for each block from the kinetic and potential contributions evaluated as time averages

$$\begin{aligned}
\boldsymbol{\sigma}(\boldsymbol{x}) &= \boldsymbol{\sigma}^K(\boldsymbol{x}) + \boldsymbol{\sigma}^V(\boldsymbol{x}), \\
\boldsymbol{\sigma}^K(\boldsymbol{x}) &= -\frac{1}{N_T}\sum_{i=1}^{N_T}\left[\sum_{\alpha} m^\alpha w\left(\boldsymbol{x}; \boldsymbol{r}_i^\alpha - \boldsymbol{x}\right)\ \boldsymbol{v}_i^\alpha \otimes \boldsymbol{v}_i^\alpha\right], \\
\boldsymbol{\sigma}^V(\boldsymbol{x}) &= \frac{1}{2N_T}\sum_{i=1}^{N_T}\left[\sum_{\alpha,\beta(\neq\alpha)} \boldsymbol{f}_i^{\alpha\beta} \otimes \boldsymbol{r}_i^{\alpha\beta}\ B\left(\boldsymbol{x}; \boldsymbol{r}_i^\alpha, \boldsymbol{r}_i^\beta\right)\right],
\end{aligned}$$

where m^α, $\boldsymbol{r}_i^\alpha$, $\boldsymbol{v}_i^\alpha$ and $\boldsymbol{f}_i^{\alpha\beta}$ are the masses, positions, velocities, and pairwise forces at time-step i, and N_T is the total number of time-steps. The symbol $\otimes$ denotes the dyadic product, e.g. $\boldsymbol{v}_i^\alpha \otimes \boldsymbol{v}_i^\alpha$ is a second-order tensor. The functions $w\left(\boldsymbol{x}; \boldsymbol{r}_i^\alpha - \boldsymbol{x}\right)$ and $B\left(\boldsymbol{x}; \boldsymbol{r}_i^\alpha, \boldsymbol{r}_i^\beta\right)$ are weighting functions that spatially average the point-wise contributions onto the discretized volume (see Vanegas et al.[30] for a more detailed discussion). Grid spacing along the direction normal to the interface, z, was 0.1 nm. For systems simulated with long range electrostatic interactions using the PME method, electrostatic contributions to the local stress were computed using a plain cut-off with a radius of 2.2 nm as reciprocal-space forces calculated with Ewald methods cannot be decomposed into pairwise central terms.[30] All local stress calculations were performed with the GROMACS-LS and MDStress library packages.[59]

Forces from torsional potentials with planar dihedral configurations ($\phi = 0, \pm 180^\circ$) cannot be decomposed into central pairwise terms as these forces would act completely within the plane, while the net forces acting on each particle are normal to the plane. This is typically not an issue as periodic torsional potentials are most often parametrized with extrema, where $\boldsymbol{F}_i = -\partial V / \partial \boldsymbol{r}_i = 0$, at planar configurations, and harmonic torsional potentials, often used to fix the chirality of a carbon center, keep the dihedral angle from visiting planar arrangements. In the case of C36, one of the headgroup torsional potential terms (O11-C1-C2-O21) has minima at $\phi = -60^\circ, 120^\circ$ and maxima at $\phi = -150^\circ, 30^\circ$ (Fig.

Results and Discussion

Interfacial Tensions in Atomistic Models

We characterize the local mechanical properties of atomistic lipid bilayers through lateral stress calculations of the commonly employed phosphocholine lipids DPPC and POPC simulated at at 50 °C (above the DPPC T_m). Comparison of the GROMOS 43A1-S3 and CHARMM36 membranes shows striking differences in the balance of repulsive and attractive stresses across the membrane (Fig.

We further explore the local balance of forces at the hydrocarbon-water interface in the C36 membrane by switching the water model from the modified mTIP3P water (default in the C36 lipid FF), that includes van der Waals (VdW) parameters on H atoms, to the standard sTIP3P water. When the same DPPC membrane is simulated with C36/sTIP3P it becomes drastically condensed, going from an area per lipid $> 60\,^2$ to $\sim 52\,^2$ (see Table

Table 1. Area per lipid, A_{L}, for atomistic membranes simulated at 50 °C.

Force-field	DPPC (^{2})	POPC (^{2})
G43A1-S3	63.8 ± 1.0	65.2 ± 0.9
C36/mTIP3P	60.4 ± 1.2	66.4 ± 1.2
C36/sTIP3P (NPT)	51.7 ± 0.7	63.9 ± 1.1
C36/sTIP3P (NP_zAT)	62.1	66.9

We delve into the role of water parametrization in the observed membrane stress profiles by simulating the three atomistic water models (SPCE, mTIP3P, and sTIP3P) at a simple liquid-vacuum interface as shown in Fig.

Returning to the membrane stress profiles, we analyze the results for atomistic POPC membranes. The stress profile for POPC with G43A1-S3 (Fig.

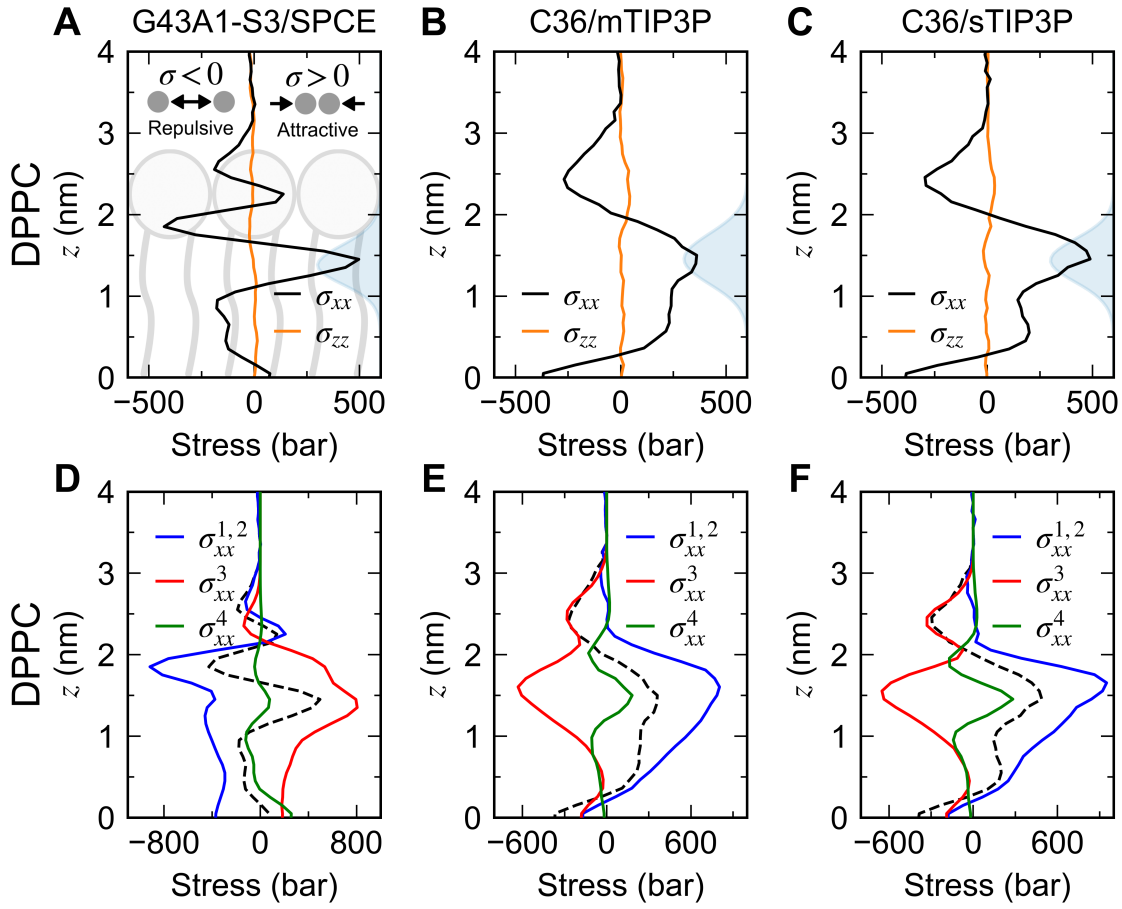

Figure 1. Lateral stress profiles of atomistic DPPC membranes simulated with GROMOS 43A1-S3/SPCE (A), CHARMM36/mTIP3P (B), and CHARMM36/sTIP3P NP_zAT (C) FFs at 50 °C. Density plot of the hydrocarbon-water interface (filled light-blue area, in arbitrary units), obtained from the overlap of water and lipid tail densities, $\rho_{\text{water}}(z) \cdot \rho_{\text{tails}}(z)$, shown on the right of each plot to guide the reader. Bottom row panels (D-F) show the corresponding lateral stress contributions from particle velocities and 2-body potentials ($\sigma^{1,2}_{xx}$, blue line), 3-body (σ^{3}_{xx}, red line) and 4-body (σ^{4}_{xx}, green line) potentials. Total lateral stress, σ_{xx}, shown in black dashed line for reference.

Table 2. Surface tension of simple liquid water-vacuum interfaces simulated at 50 °C.

System	Tension (mN/m)
Expt.[a]	67.9 ± 0.3
SPCE	56.1 ± 1.8
mTIP3P	47.7 ± 1.7
sTIP3P	43.5 ± 1.7
MARTINI	30.5 ± 1.1
Pol-MARTINI	28.9 ± 1.2
BMW	75.7 ± 1.4

[a]Data from Vargaftik et al.[61]

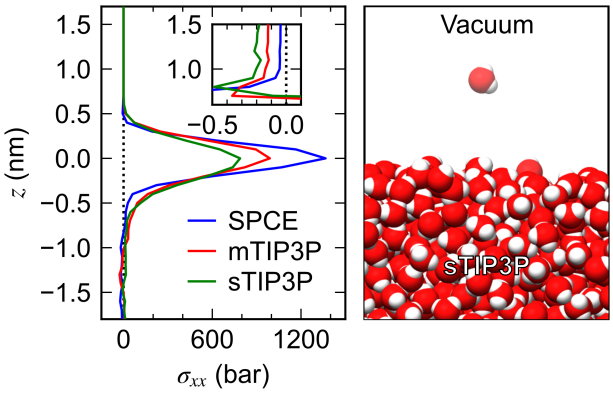

Figure 2. Lateral stress profiles of liquid water-vacuum interfaces simulated with atomistic SPCE, mTIP3P, and sTIP3P models. Illustration on the right shows a snapshot of the interface.

Explicit and Implicit Solvent in CG Bilayers

In the previous section, our results showed how subtle differences in the parametrization of water can lead to large effects in interfacial properties. We now turn our attention to CG models including the explicit solvent MARTINI, Pol-MARTINI, and BMW-MARTINI FFs as well as the solvent-free Dry-MARTINI. We first focus our attention on lateral stress profiles at the simple liquid-vacuum interface as shown in Fig.

Stress profiles for DPPC and POPC membranes simulated with the various MARTINI FFs are shown in Fig.

Unlike the atomistic models discussed in the previous section, the stress profiles of CG MARTINI DPPC and POPC membranes are very similar. This is not unexpected given that CG models aim only to describe general chemical features and in MARTINI, the only distinction between DPPC and POPC is the VdW parametrization for the middle bead in the SN2 chain. However, the significant variations observed in the stress profiles of the atomistic models reflect important physical differences between the two lipids such as melting transition temperatures, $T_m = -2°\text{C}$ for POPC compared to $T_m = -41°\text{C}$ for DPPC despite the longer chain length. Additionally, mechanical properties such as the bending elasticity modulus of a fluid bilayer decreases with the number of unsaturations in the lipid tails, while the lateral area compressibility remains practically unchanged.[63,64]

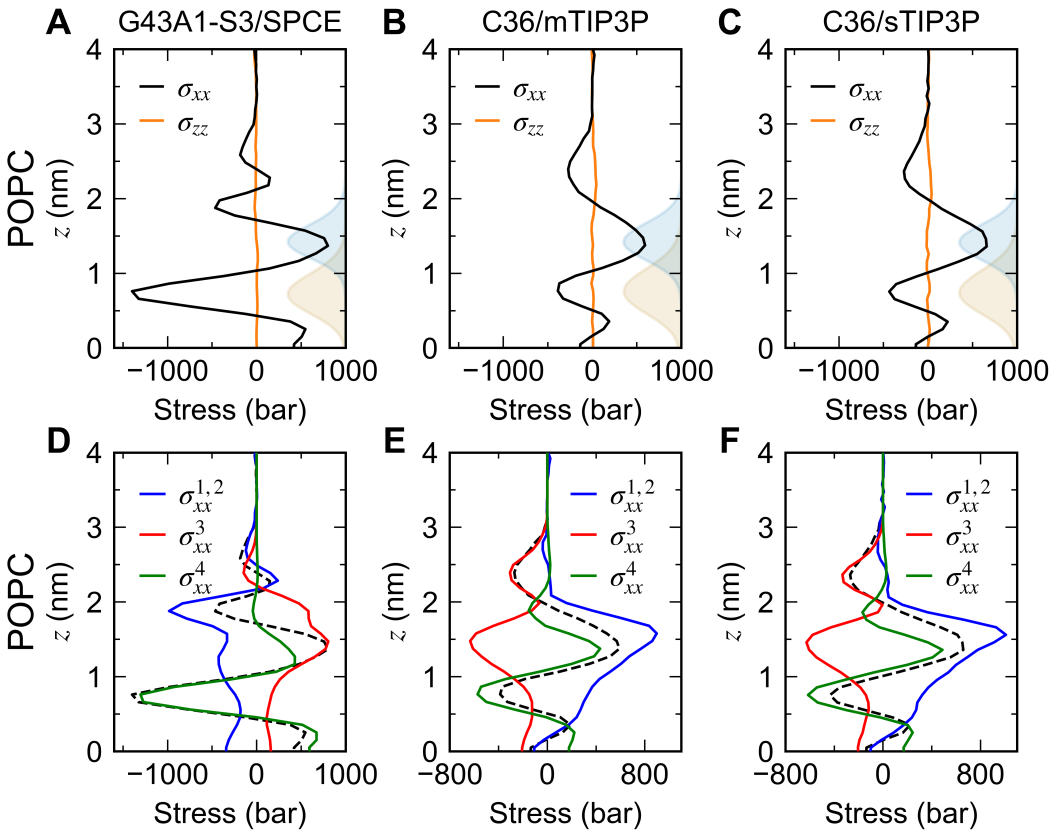

Figure 3. Lateral stress profiles of atomistic POPC membranes simulated with GROMOS 43A1-S3/SPCE FF (A), CHARMM36/mTIP3P (B), and CHARMM36/sTIP3P NP_zAT (C) at 50 °C. Density plot of the hydrocarbon-water interface (filled light-blue area, in arbitrary units), obtained from the overlap of water and lipid tail densities, $\rho_{\text{water}}(z) \cdot \rho_{\text{tails}}(z)$, shown on the right of each plot to guide the reader. Density plot of the *cis* double bond atoms shown in light tan color. Bottom row panels (D-F) show the corresponding lateral stress contributions from particle velocities and 2-body potentials ($\sigma_{xx}^{1,2}$, blue line), 3-body (σ_{xx}^{3}, red line) and 4-body (σ_{xx}^{4}, green line) potentials. Total lateral stress, σ_{xx}, shown in black dashed line for reference.

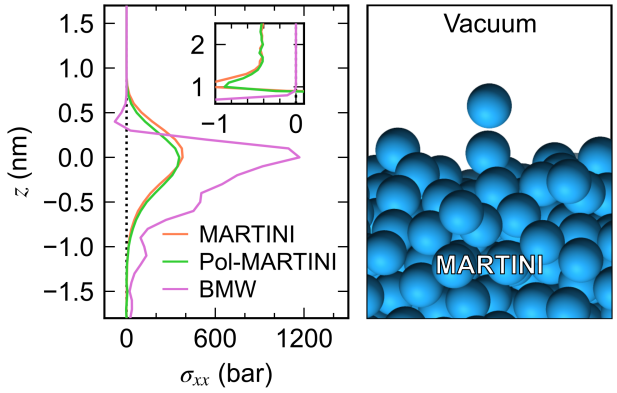

Figure 4. Lateral stress profiles of liquid water-vacuum interfaces simulated with coarse-grained non-polar single bead MARTINI, three-point polarizable water (Pol-MARTINI), and big multipole water model (BMW) models. Illustration on the right shows a snapshot of the interface.

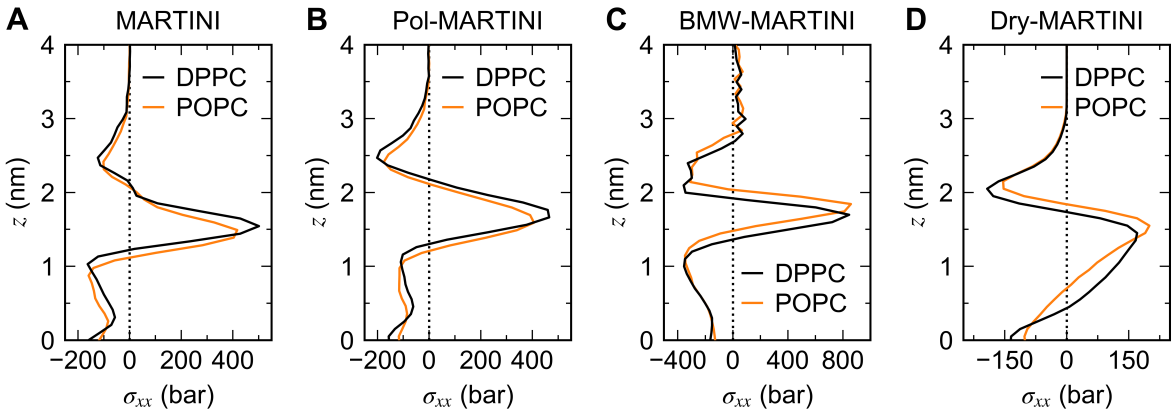

Figure 5. Lateral stress profiles of coarse-grained membranes simulated with the MARTINI FF under a variety of solvent treatments including non-polar single bead MARTINI (A), three-point polarizable water Pol-MARTINI (B), big multipole water model BMW-MARTINI (C), and solvent-free Dry-MARTINI (D).

Effects of Stress Profile Shape on Macroscopic Elastic Properties

The lateral stress and elastic modulus profiles provide microscopic underpinnings of material parameters through various combinations of integral moments (of degree $n = 0, 1$, or 2),

$$[\![X]\!]_{n,\mathrm{m}} = \int dz (z - z_0)^n X(z), \tag{2}$$

where the subscript m (or b) denotes whether the integral is computed over the width of a monolayer or the entire bilayer and z_0 is the position of the pivotal plane. For a monolayer, z_0 is expected to be located near the hydrocarbon-water interface and for a bilayer it is located at the midplane. The two most commonly described monolayer elastic constants, the bending (κ_m) and Gaussian curvature ($\bar{\kappa}_\mathrm{m}$) moduli, are defined as follows based on the recent quadratic curvature-tilt theory of Terzi, Ergüder and Deserno,[19]

$$\kappa_\mathrm{m} = [\![\lambda_\mathrm{L}]\!]_{2,\mathrm{m}} - [\![\sigma_\mathrm{L}]\!]_{2,\mathrm{m}} + [\![\lambda_\mathrm{S}]\!]_{2,\mathrm{m}}, \tag{3}$$

$$\bar{\kappa}_\mathrm{m} = [\![\sigma_\mathrm{L}]\!]_{2,\mathrm{m}} - 2[\![\lambda_\mathrm{S}]\!]_{2,\mathrm{m}}. \tag{4}$$

The quantities λ_L and λ_S refer to the lateral stretch and shear modulus profiles respectively. The last term on the right hand side of Eq. 3 defines the lipid twist modulus, $\kappa_{\mathrm{tw,m}} = [\![\lambda_\mathrm{S}]\!]_{2,\mathrm{m}}$, which, having values in the order of $\sim 5\ k_\mathrm{B}T$ per monolayer,[19] provides non-trivial contributions to both κ_m and $\bar{\kappa}_\mathrm{m}$. Earlier theories that ignored the lipid twist term defined the bilayer Gaussian modulus directly from the second moment of the stress profile, $\bar{\kappa} = [\![\sigma_\mathrm{L}]\!]_{2,\mathrm{b}}$.[16] While it may be possible to obtain λ_L, λ_S, and z_0 directly from the microscopic elasticity tensor[16,17] (λ_{ijkl}, computed from spatial fluctuations in the microscopic stress tensor[65]), these are non-trivial calculations that are beyond the scope of this paper. Nonetheless, we can get a glimpse of how the shape of the lateral stress profiles will affect macroscopic elastic properties by calculating the second moment over the bilayer, $[\![\sigma_\mathrm{L}]\!]_{2,\mathrm{b}}$. Values of $[\![\sigma_\mathrm{L}]\!]_{2,\mathrm{b}}$ for

all the atomistic and CG membranes simulated are shown in Table

Table 3. Second moment of bilayer stress profiles, $[\![\sigma_{\mathrm{L}}]\!]_{2,\mathrm{b}}$.

Force-field	DPPC ($k_{\mathrm{B}}T$)	POPC ($k_{\mathrm{B}}T$)
G43A1-S3/SPCE	-20.7 ± 1	-15.1 ± 1.6
C36/mTIP3P	-42.9 ± 0.5	-14.6 ± 1.9
C36/sTIP3P (NP_zAT)	-24.9 ± 0.5	-15.5 ± 0.2
MARTINI	0.4 ± 0.3	1.9 ± 0.3
Pol-MARTINI	-8.2 ± 0.7	-5.4 ± 0.7
BMW-MARTINI	5.1 ± 5.3	8.2 ± 0.6
Dry-MARTINI	-11.8 ± 0.1	-7.0 ± 0.1

For reference, the Gaussian curvature modulus for a planar membrane is expected to be negative and of the same order as the bending modulus,[19] which experiments place this value to be in the range of 10 – 40 $k_{\mathrm{B}}T$ for POPC bilayers in the fluid phase.[66] Most of the values in Table

For the atomistic systems, we see the greatest difference in $[\![\sigma_{\mathrm{L}}]\!]_{2,\mathrm{b}}$ for the C36/mTIP3P DPPC bilayer whose value of $-42.9\ k_{\mathrm{B}}T$ is 2× that of G43A1-S3/SPCE ($-20.7\ k_{\mathrm{B}}T$) and 1.7× that of C36/sTIP3P ($-24.9\ k_{\mathrm{B}}T$). This is in contrast to the values obtained for POPC that are essentially the same for all three atomistic systems ($\approx -15\ k_{\mathrm{B}}T$). The Dry-MARTINI DPPC membrane has the most negative value of $[\![\sigma_{\mathrm{L}}]\!]_{2,\mathrm{b}}$ in the CG simulations, which is consistent with the similar stress distribution as observed for C36/mTIP3P DPPC. Together, these numerical results indicate that the local distribution of repulsive and attractive stresses across the bilayer will affect macroscopic observables even though there is an overall balance of forces as the simulated bilayers are tensionless.

Conclusions

Here, we have characterized the local mechanical properties of liquid water and membrane interfaces through analysis of lateral stress profiles from MD simulations. Our results show that different force-field descriptions of water and lipid interactions can lead to drastically

different overall balance of forces. We observe large variations in interfacial tensions, both locally and totally, between the different CG and atomistic water models. In the case of all-atom FFs, the balance of pairwise, e.g., coulomb and VdW, and multibody interactions can lead to unexpected differences in water-vacuum and hydrocarbon-water tensions, which may partly contribute to the observation that DPPC simulated with C36/mTIP3P displays a broad attractive stress that spans the interface and most of the lipid tail region. The conventional expectation is that unfavorable hydrophobic forces between water and hydrocarbon tails should lead to a narrow attractive surface tension just below the headgroup region, as observed in the water-vacuum simulations, while configurational entropy of the tails should lead to repulsive stresses in the bilayer core.[12,33] Comparison of the CG and atomistic models, e.g., G43A1-S3 vs. MARTINI and C36 vs. Dry-MARTINI, suggests that various parametrization strategies converge to similar local stress states despite vast differences in the potentials. Numerical integration of the second moment of the stress profiles in the last section shows that one can expect a broad range of macroscopic elastic properties depending on the local distribution of repulsive and attractive stresses across the membrane that arises from each force-field parametrization.

Computational models must always strike a compromise between numerical efficiency and capturing physical properties of interest such as the hydrophobic effect. For instance, it is common practice to truncate VdW interactions at a cutoff radius of 1.0 or 1.2 nm with the argument that the potential becomes negligibly small beyond this distance and therefore it can be safely discarded. However, this may not be an adequate choice for non-polar hydrocarbons or liquid-crystalline systems, where relatively small VdW forces beyond 1.2 nm may contribute significantly when added up over many neighboring molecules. Chiu et al.[35] pointed out that a VdW cutoff radius of at least 1.5 nm was needed in order to create a hydrocarbon FF that was transferable across alkane chains of various lengths during the parametrization of G43A1-S3. Similarly, a recent analysis of the C36 and CHARMM Drude polarizable FFs found that incorporation of long-range VdW interactions, either by

using long cutoffs or Lennard-Jones PME, improved significantly the accuracy of alkane simulations when compared to experimental quantities such as surface tension.[67] One should note however, that simply adding LJ-PME to C36 or any other lipid FF without re-adjusting the parameters would likely lead to over-condensation of the membrane due to the increased attractive forces.

While macroscopic surface tension is often used to gauge the quality of liquid force-fields, experimental values of tension are not typically incorporated during parametrization. This should be reconsidered, and local as well as global 'mechanical' properties of biomolecules and liquid interfaces should be included in the FF development process. An example of such an approach is the recently developed 3-site water model, TIP3P-ST, by Qiu et al.[68] that is able to correctly reproduce the temperature of maximum density of water for the first time, although with less accurate transport properties compared to other models, by using experimental surface tension data. Water is an essential component of all biomolecular simulation FFs and more accurate yet numerically efficient water models such as TIP3P-ST, TIP3P-FB,[69] or OPC3[70,71] should be considered to replace the now three-decade old TIP3P and SPCE models in future FF parametrizations. Beyond reproducing interfacial effects, atomistic and to some extent CG computational models must also accurately represent the micro and macroscopic physical properties of molecular features such as lipid unsaturations. Our analysis shows a large variation in the numerical description of the rigid *cis* double bond as large repulsive stresses are observed in the hydrophobic core region of the atomistic POPC systems, with the G43A1-S3 peak being $\sim 3\times$ as large compared to C36, while the MARTINI stress profiles show minimal differences between DPPC and POPC. This last point should be considered within the context of fluorescence experiments[34] that indicate that the lateral stress at the position of the *cis* double bond in the doubly-unsaturated DOPC may be very different than in other locations along the hydrocarbon chain.

Acknowledgement

JMV acknowledges the support of the National Science Foundation through grant No. CHE-1944892. Computations were performed, in part, on the Vermont Advanced Computing Core supported in part by NSF award No. OAC-1827314.

References

(1) Chernomordik, L. V.; Kozlov, M. M. Mechanics of Membrane Fusion. *Nat. Struct. Mol. Biol.* **2008**, *15*, 675–683.

(2) McMahon, H. T.; Boucrot, E. Membrane Curvature at a Glance. *J. Cell. Sci.* **2015**, *128*, 1065–1070.

(3) Behnia, R.; Munro, S. Organelle Identity and the Signposts for Membrane Traffic. *Nature* **2005**, *438*, 597–604.

(4) Haswell, E. S.; Phillips, R.; Rees, D. C. Mechanosensitive Channels: What Can They Do and How Do They Do It? *Structure* **2011**, *19*, 1356–1369.

(5) Anishkin, A.; Loukin, S. H.; Teng, J.; Kung, C. Feeling the Hidden Mechanical Forces in Lipid Bilayer Is an Original Sense. *Proc. Natl. Acad. Sci. USA* **2014**, *111*, 7898–7905.

(6) Lam, R. M.; Chesler, A. T. Shear Elegance: A Novel Screen Uncovers a Mechanosensitive GPCR. *J. Gen. Physiol.* **2018**, *150*, 907–910.

(7) Xu, J.; Mathur, J.; Vessières, E.; Hammack, S.; Nonomura, K.; Favre, J.; Grimaud, L.; Petrus, M.; Francisco, A.; Li, J. et al. GPR68 Senses Flow and Is Essential for Vascular Physiology. *Cell* **2018**, *173*, 762–775.

(8) Ranade, S. S.; Qiu, Z.; Woo, S. H.; Hur, S. S.; Murthy, S. E.; Cahalan, S. M.; Xu, J.; Mathur, J.; Bandell, M.; Coste, B. et al. Piezo1, a Mechanically Activated Ion Channel,

Is Required for Vascular Development in Mice. *Proc. Natl. Acad. Sci. USA* **2014**, *111*, 10347–10352.

(9) Ranade, S. S.; Woo, S.-H.; Dubin, A. E.; Moshourab, R. A.; Wetzel, C.; Petrus, M.; Mathur, J.; Bégay, V.; Coste, B.; Mainquist, J. et al. Piezo2 Is the Major Transducer of Mechanical Forces for Touch Sensation in Mice. *Nature* **2015**, *516*, 121–125.

(10) Kocer, A. Mechanisms of Mechanosensing-Mechanosensitive Channels, Function and Re-Engineering. *Curr. Opin. Chem. Biol.* **2015**, *29*, 120–127.

(11) Brohawn, S. G. How Ion Channels Sense Mechanical Force: Insights From Mechanosensitive K2P Channels TRAAK, TREK1, and TREK2. *Ann. N.Y. Acad. Sci.* **2015**, *1352*, 20–32.

(12) Marsh, D. Lateral Pressure Profile, Spontaneous Curvature Frustration, and the Incorporation and Conformation of Proteins in Membranes. *Biophys. J.* **2007**, *93*, 3884–3899.

(13) Helfrich, W.; Kozlov, M. M. Bending Tensions and the Bending Rigidity of Fluid Membranes. *J. Phys. II France* **1993**, *3*, 287–292.

(14) Helfrich, W. Elastic Properties of Lipid Bilayers: Theory and Possible Experiments. *Z. Naturforsch.* **1973**, *28c*, 693–703.

(15) Ben-Shaul, A.; Szleifer, I.; Gelbart, W. M. Statistical Thermodynamics of Amphiphile Chains in Micelles. *P. Natl. Acad. Sci. USA* **1984**, *81*, 4601–4605.

(16) Hamm, M.; Kozlov, M. M. Elastic Energy of Tilt and Bending of Fluid Membranes. *Eur. Phys. J. E* **2000**, *3*, 323–335.

(17) Campelo, F.; Arnarez, C.; Marrink, S. J.; Kozlov, M. M. Helfrich Model of Membrane Bending: From Gibbs Theory of Liquid Interfaces to Membranes as Thick Anisotropic Elastic Layers. *Adv. Coll. Interf. Sci.* **2014**, *208*, 25–33.

(18) Terzi, M. M.; Deserno, M. Novel Tilt-Curvature Coupling in Lipid Membranes. *J. Chem. Phys.* **2017**, *147*, 084702.

(19) Terzi, M. M.; Ergüder, M. F.; Deserno, M. A Consistent Quadratic Curvature-Tilt Theory for Fluid Lipid Membranes. *J. Chem. Phys.* **2019**, *151*, 164108.

(20) Cantor, R. S. The Lateral Pressure Profile in Membranes: A Physical Mechanism of General Anesthesia. *Biochemistry-US* **1997**, *36*, 2339–2344.

(21) Ollila, O. H. S.; Risselada, H.; Louhivuori, M.; Lindahl, E.; Vattulainen, I.; Marrink, S. 3D Pressure Field in Lipid Membranes and Membrane-Protein Complexes. *Phys. Rev. Lett.* **2009**, *102*, 1–4.

(22) Cantor, R. S. Lipid Composition and the Lateral Pressure Profile in Bilayers. *Biophys. J.* **1999**, *76*, 2625–2639.

(23) Irving, J. H.; Kirkwood, J. G. The Statistical Mechanical Theory of Transport Processes. IV. The Equations of Hydrodynamics. *J. Chem. Phys.* **1950**, *18*, 817–829.

(24) Noll, W. Die Herleitung der Grundgleichungen der Thermomechanik der Kontinua aus der Statistischen Mechanik. *J. Natural Mech. and Anal.* **1955**, *4*, 627–646.

(25) Hardy, R. J. Formulas for Determining Local Properties in Molecular-Dynamics Simulations: Shock Waves. *J. Chem. Phys.* **1982**, *76*, 622–628.

(26) Murdoch, A. I. The Motivation of Continuum Concepts and Relations From Discrete Considerations. *Q. J. Mech. Appl. Math.* **1983**, *36*, 163–187.

(27) Schofield, P.; Henderson, J. Statistical Mechanics of Inhomogeneous Fluids. *Proc. R. Soc. Lond. A* **1982**, *379*, 231–246.

(28) Goetz, R.; Lipowsky, R. Computer Simulations of Bilayer Membranes: Self-Assembly and Interfacial Tension. *J. Chem. Phys.* **1998**, *108*, 7397–7409.

(29) Admal, N. C.; Tadmor, E. B. A Unified Interpretation of Stress in Molecular Systems. *J. Elast.* **2010**, *100*, 63–143.

(30) Vanegas, J. M.; Torres-Sánchez, A.; Arroyo, M. Importance of Force Decomposition for Local Stress Calculations in Biomembrane Molecular Simulations. *J. Chem. Theory Comput.* **2014**, *10*, 691–702.

(31) Torres-Sánchez, A.; Vanegas, J. M.; Arroyo, M. Examining the Mechanical Equilibrium of Microscopic Stresses in Molecular Simulations. *Phys. Rev. Lett.* **2015**, *114*, 258102.

(32) Torres-Sánchez, A.; Vanegas, J. M.; Arroyo, M. Geometric Derivation of the Microscopic Stress: A Covariant Central Force Decomposition. *J. Mech. Phys. Solids* **2016**, *93*, 224–239.

(33) Ting, C. L.; Müller, M. Membrane Stress Profiles From Self-Consistent Field Theory. *J. Chem. Phys.* **2017**, *146*, 104901.

(34) Templer, R. H.; Castle, S. J.; Curran, A. R.; Rumbles, G.; Klug, D. R. Sensing Isothermal Changes in the Lateral Pressure in Model Membranes Using Di-Pyrenyl Phosphatidylcholine. *Faraday Discuss.* **1998**, *111*, 41–53.

(35) Chiu, S.-W.; Pandit, S. A.; Scott, H. L.; Jakobsson, E. An Improved United Atom Force Field for Simulation of Mixed Lipid Bilayers. *J. Phys. Chem. B* **2009**, *113*, 2748–2763.

(36) Klauda, J. B.; Venable, R. M.; Freites, J. A.; O'Connor, J. W.; Tobias, D. J.; Mondragon-Ramirez, C.; Vorobyov, I.; Mackerell, A. D.; Pastor, R. W. Update of the CHARMM All-Atom Additive Force Field for Lipids: Validation on Six Lipid Types. *J. Phys. Chem. B* **2010**, *2*, 7830–7843.

(37) Pastor, R. W.; Mackerell, A. D. Development of the CHARMM Force Field for Lipids. *J. Phys. Chem. Lett.* **2011**, *2*, 1526–1532.

(38) Braun, A. R.; Sachs, J. N.; Nagle, J. F. Comparing Simulations of Lipid Bilayers to Scattering Data: The GROMOS 43A1-S3 Force Field. *J. Phys. Chem. B* **2013**, *117*, 5065–5072.

(39) Jämbeck, J. P. M.; Lyubartsev, A. P. Derivation and Systematic Validation of a Refined All-Atom Force Field for Phosphatidylcholine Lipids. *J. Phys. Chem. B* **2012**, *116*, 3164–3179.

(40) Berger, O.; Edholm, O.; Jähnig, F. Molecular Dynamics Simulations of a Fluid Bilayer of Dipalmitoylphosphatidylcholine at Full Hydration, Constant Pressure, and Constant Temperature. *Biophys. J.* **1997**, *72*, 2002–2013.

(41) Dickson, C. J.; Madej, B. D.; Skjevik, . A.; Betz, R. M.; Teigen, K.; Gould, I. R.; Walker, R. C. Lipid14: The Amber Lipid Force Field. *J. Chem. Theory Comput.* **2014**, *10*, 865–879.

(42) Berendsen, H. J. C.; Grigera, J. R.; Straatsma, T. P. The Missing Term in Effective Pair Potentials. *J. Phys. Chem.* **1987**, *91*, 6269–6271.

(43) Jorgensen, W. L.; Chandrasekhar, J.; Madura, J. D.; Impey, R. W.; Klein, M. L. Comparison of Simple Potential Functions for Simulating Liquid Water. *J. Chem. Phys.* **1983**, *79*, 926–935.

(44) Marrink, S. J.; Risselada, H. J.; Yefimov, S.; Tieleman, D. P.; de Vries, A. H. The MARTINI Force Field: Coarse Grained Model for Biomolecular Simulations. *J. Phys. Chem. B* **2007**, *111*, 7812–7824.

(45) Sodt, A. J.; Head-Gordon, T. An Implicit Solvent Coarse-Grained Lipid Model With Correct Stress Profile. *J. Chem. Phys.* **2010**, *132*, 205103–205111.

(46) Orsi, M.; Michel, J.; Essex, J. W. Coarse-Grain Modelling of DMPC and DOPC Lipid Bilayers. *J. Phys.: Condens. Matter* **2010**, *22*, 155106–155121.

(47) Marrink, S. J.; de Vries, A. H.; Mark, A. E. Coarse Grained Model for Semiquantitative Lipid Simulations. *J. Phys. Chem. B* **2004**, *108*, 750–760.

(48) Yesylevskyy, S. O.; Schäfer, L. V.; Sengupta, D.; Marrink, S. J. Polarizable Water Model for the Coarse-Grained MARTINI Force Field. *PLoS Comput. Biol.* **2010**, *6*, e1000810.

(49) Wu, Z.; Cui, Q.; Yethiraj, A. A New Coarse-Grained Model for Water: The Importance of Electrostatic Interactions. *J. Phys. Chem. B* **2010**, *114*, 10524–10529.

(50) Wu, Z.; Cui, Q.; Yethiraj, A. A New Coarse-Grained Force Field for Membrane-Peptide Simulations. *J. Chem. Theory Comput.* **2011**, 3793–3802.

(51) Arnarez, C.; Uusitalo, J. J.; Masman, M. F.; Ingólfsson, H. I.; de Jong, D. H.; Melo, M. N.; Periole, X.; de Vries, A. H.; Marrink, S. J. Dry Martini, a Coarse-Grained Force Field for Lipid Membrane Simulations with Implicit Solvent. *J. Chem. Theory Comput.* **2015**, *11*, 260–275.

(52) Hess, B.; Kutzner, C.; van Der Spoel, D.; Lindahl, E. GROMACS 4: Algorithms for Highly Efficient, Load-Balanced, and Scalable Molecular Simulation. *J. Chem. Theory Comput.* **2008**, *4*, 435–447.

(53) Pronk, S.; Páll, S.; Schulz, R.; Larsson, P.; Bjelkmar, P.; Apostolov, R.; Shirts, M. R.; Smith, J. C.; Kasson, P. M.; van der Spoel, D. et al. GROMACS 4.5: A High-Throughput and Highly Parallel Open Source Molecular Simulation Toolkit. *Bioinformatics* **2013**, *29*, 845–854.

(54) Abraham, M. J.; Murtola, T.; Schulz, R.; Páll, S.; Smith, J. C.; Hess, B.; Lindahl, E. GROMACS: High Performance Molecular Simulations Through Multi-Level Parallelism From Laptops to Supercomputers. *SoftwareX* **2015**, *1-2*, 19–25.

(55) Bussi, G.; Donadio, D.; Parrinello, M. Canonical Sampling Through Velocity Rescaling. *J. Chem. Phys.* **2007**, *126*, 014101.

(56) Hardy, R.; Root, S.; Swanson, D. Continuum Properties From Molecular Simulations. *AIP Conf. Proc.* **2002**, 7–10.

(57) Murdoch, A. I. A Critique of Atomistic Definitions of the Stress Tensor. *J. Elast.* **2007**, *88*, 113–140.

(58) Tadmor, E. B.; Miller, R. E. *Modeling Materials: Continuum, Atomistic and Multiscale Techniques*; Cambridge University Press: New York, 2011.

(59) Vanegas, J. M.; Torres-Sánchez, A.; Arroyo, M. MDStress: Computational Tools for Local Stress Calculations From Molecular Simulations. (accessed July 14, 2020); `http://mdstress.org`.

(60) Boonstra, S.; Onck, P. R.; Giessen, E. v. d. CHARMM TIP3P Water Model Suppresses Peptide Folding by Solvating the Unfolded State. *J. Phys. Chem. B* **2016**, *120*, 3692–3698.

(61) Vargaftik, N. B.; Volkov, B. N.; Voljak, L. D. International Tables of the Surface Tension of Water. *J. Phys. Chem. Ref. Data* **1983**, *12*, 817–820.

(62) Srivastava, A.; Voth, G. a. Hybrid Approach for Highly Coarse-Grained Lipid Bilayer Models. *J. Chem. Theory Comput.* **2013**, *9*, 750–765.

(63) Rawicz, W.; Olbrich, K.; McIntosh, T. Effect of Chain Length and Unsaturation on Elasticity of Lipid Bilayers. *Biophys. J.* **2000**, *79*, 328–339.

(64) Marsh, D. Elastic Curvature Constants of Lipid Monolayers and Bilayers. *Chem. Phys. Lipids* **2006**, *144*, 146–159.

(65) Lips, D.; Maass, P. Stress-Stress Fluctuation Formula for Elastic Constants in the *NPT* Ensemble. *Phys. Rev. E* **2018**, *97*, 1–9.

(66) Dimova, R. Recent Developments in the Field of Bending Rigidity Measurements on Membranes. *Adv. Colloid Interfac.* **2014**, *208*, 225–234.

(67) Leonard, A. N.; Simmonett, A. C.; Pickard IV, F. C.; Huang, J.; Venable, R. M.; Klauda, J. B.; Brooks, B. R.; Pastor, R. W. Comparison of Additive and Polarizable Models with Explicit Treatment of Long-Range Lennard-Jones Interactions Using Alkane Simulations. *J. Chem. Theory Comput.* **2018**, *14*, 948–958.

(68) Qiu, Y.; Nerenberg, P. S.; Head-Gordon, T.; Wang, L.-P. Systematic Optimization of Water Models Using Liquid/Vapor Surface Tension Data. *J. Phys. Chem. B* **2019**, *123*, 7061–7073.

(69) Wang, L.-P.; Martinez, T. J.; Pande, V. S. Building Force Fields: An Automatic, Systematic, and Reproducible Approach. *J. Phys. Chem. Lett.* **2014**, *5*, 1885–1891.

(70) Izadi, S.; Onufriev, A. V. Accuracy Limit of Rigid 3-Point Water Models. *J. Chem. Phys.* **2016**, *145*, 074501–11.

(71) Izadi, S.; Anandakrishnan, R.; Onufriev, A. V. Building Water Models: A Different Approach. *J. Phys. Chem. Lett.* **2014**, *5*, 3863–3871.

Graphical TOC Entry